The Closed State of the Shaker Potassium Channel and the Mechanism of Voltage Activation

Richa Agrawal[1,2], Ramon Mendoza Uriarte[3], Bernardo Pinto Anwandter[1], Trayder Thomas[1], Younghoon Koh[1], Lydia Blachowicz[1], Francisco Bezanilla[1], Eduardo Perozo[1,2*], and Benoît Roux[1,3*]

1. Department of Biochemistry and Molecular Biology, The University of Chicago, Chicago, 60637, IL, USA
2. Center for Mechanical Excitability, The University of Chicago, Chicago, 60637, IL, USA
3. Department of Chemistry, The University of Chicago, Chicago, 60637, IL, USA

* Email: roux@uchicago.edu, eperozo@uchicago.edu

ABSTRACT

Voltage-gated potassium (Kv) channels play a critical role in cellular excitability and the propagation of the nerve impulse. Despite the extensive amount of information available about Kv channels, the complete process of voltage activation—where a conformational change mediated by voltage-sensor domains (VSD) opens the intracellular gate in response to the depolarization of the membrane potential—has not been fully elucidated. To understand this process, we study the Kv Shaker channel and focus on the ILT mutant (V369I, I372L, S376T) known to display a long-lived closed intermediate state during the activation process. Single particle CryoEM of the ILT mutant reveals a novel conformation of Shaker in which the intracellular gate formed by the S5-S6 helices is in a closed state and the S4 helix in the VSD is in an intermediate state shifted down by ~5Å relative to its position in the fully activated open channel. Additional conformations of the channel generated by Alphafold2 and molecular dynamics simulations are used to map the sequence of intermediate states along the voltage activation process, revealing the nature of the couping between the VSD, the S4-S5 linker, and the S5-S6 intracellular gate. In the final stage of the activation process, as the VSD reaches its fully activated conformation while the gate remains closed, essential interactions between the S4–S5 linker and the intracellular S5-S6 gate are transiently disrupted and reformed when the gate opens, demonstrating that electro-mechanical coupling results from a dynamic shift in population equilibrium between metastable states. These findings provide unprecedented mechanistic insight into how structural rearrangements underlie the voltage activation process in Kv channels, offering broader implications for understanding channelopathies and designing targeted modulators.

INTRODUCTION

Voltage-gated potassium (Kv) channels are essential components of excitable membranes such as nerves and muscles, enabling the rapid and selective efflux of K^+ ions in response to changes in membrane potential [1,2]. Kv channels are tetrameric membrane proteins in which each subunit contains 6 transmembrane helices (S1-S6) organized into two main structural features: the S1-S4 helices forming the voltage sensor domain (VSD) that responds to changes in the membrane potential, and the S5-S6 helices forming the pore domain (PD) that comprises the ion conducting selectivity filter and the intracellular activation gate [3]. In Kv channels, the VSD undergoes a series of conformational changes driven by the translocation of conserved arginine residues along the S4 helix, ultimately leading to pore opening [4-6]. The conformational change within the VSD is thought to take place according to the sliding helix mechanism, which envisions that electrostatic forces hold down the S4 helix with its arginine gating charges at negative membrane potential, while membrane depolarization releases the S4 helix towards the extracellular side [7-9]. However, the nature of the electro-mechanical (E-M) coupling mechanism, by which the voltage-driven movement of the S4

helix in the VSD leads to the opening of the intracellular gate in the PD is not known. To resolve this issue, it is necessary to know the complete sequence of conformational states linking the closed resting state to the open activated state of a Kv channel.

However, it has been experimentally challenging to capture Kv channels in different functional states. Most of the available Kv channel structures show the open activated state, which dominates at a transmembrane potential of 0 mV. Recently, a CryoEM structure of the Shaker WT channel in the open activated state has been obtained [10]. In an attempt to determine structures of the resting and closed states of the Kv4.2 channel, a mutation of V406C in the PXP motif of the S6 helix (corresponding to Shaker V478C) has been introduced to crosslink with another subunit in the presence of Hg^{2+} [11]. In this structure, the mutation in the S6 helix alters the S4 helix and S4-S5 linker, yielding a closed gate. Structures of Kv2.1 in different conformational states have been obtained in the presence of a membrane potential in which the VSD is shifted down by ~5 Å compared to the activated state of Kv2.1 and the gate is partially closed [12]. A Shaker channel I384R mutant structure has been solved recently that shows the pore is partially closed at the intracellular region (I470, V474), while the VSD is observed to be fully activated [13]. At this point, the structures of the resting or other intermediate closed states remain unknown and our understanding of how conformational changes in the VSD are coupled to pore gating is limited.

To resolve the mechanism of voltage-activation in Kv channels, we have exploited the Shaker ILT triple mutant (V369I, I372L, S376T). These mutations localized along the S4 helix of the VSD alter the coupling between voltage-driven movements and gate opening. The latter remains closed even when moving ~90% of the total gating charge with membrane depolarization; only a highly depolarized membrane potential succeeds to move the remainder of the gating charge and open the pore [14-16]. Despite functional studies characterizing the Shaker ILT mutant, as well as models of the mutations [17,18], the structural basis for its functional phenotype remains unclear. For this reason, the ILT mutant provides a unique opportunity to capture a conformation of the channel near the final stages of voltage sensor movement and pore opening.

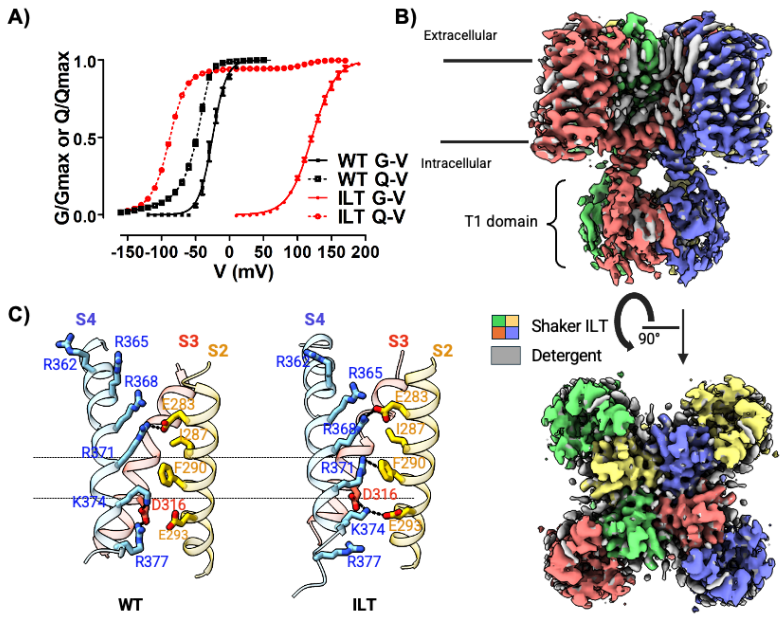

Figure 1. Structure of Shaker ILT. A) Normalized conductance (G/Gmax)-voltage curve (G-V) and normalized gating current Q/Qmax-voltage curve (Q-V); for Shaker WT (black) and Shaker ILT (red)**. B)** Side and top view of the tetramer map (sharpened) of Shaker ILT. **C)** Gating charge interactions in the voltage sensor domain for both WT (left) and ILT (right). The S2 (gold), S3 (red), and S4 (cyan) helices are shown (S1 is not shown for the sake of clarity). The two dashed lines indicate the position of the hydrophobic region of the VSD.

In this work, the structure of the Shaker ILT triple mutant was determined using single particle CryoEM. Compared with the Shaker wild type (WT) activated state structure (PDB ID: 7SIP), specific features that underlie pore closure are identified. These include the sliding motion of the S4 helix, shifts in the S4-S5 linker geometry, and changes in the VSD-PD interaction networks. Functional studies on the ILT mutant complemented by computational modeling with AlphaFold and molecular dynamics (MD) simulations are carried out to help identify other transient states along the activation pathway[8,9]. These results provide new structures of the Kv channel that elucidate a complete activation cycle from resting state to activated state. These findings provide the molecular underpinnings for an understanding of voltage activation in Kv channels.

RESULTS

Structure of Shaker ILT

While the conductance vs. voltage relationship (G-V) of the Shaker ILT mutant is strongly right-shifted to higher voltages compared to that of Shaker WT, the gating charge vs. voltage relationship (Q-V) is not strongly shifted (**Fig. 1A**). The interpretation is that the VSD is stabilized in an intermediate state with near complete gating charge preceding the final transition to the open activated state [19]. This functional phenotype was exploited to capture the channel in this intermediate conformation. The structure was determined at a resolution of 3.4 Å using single-particle cryo-EM (**Fig. 1B,** additional information in **Figs. S1** and **S2**). The structure of Shaker WT (PDB ID: 7SIP) was used as a model to build the atomic coordinates of Shaker ILT in the transmembrane region, and the structure of the Kv1.2-2.1 chimera (PDB ID: 5WIE) was used as a reference model for the T1 domain. The structure of the T1 domain, not previously reported, could also be resolved in the map. A hydrogen bond is present between the side chain of Arg487 near the end of the S6 helix and the main chain oxygen of Ile197 in the T1 domain of the same subunit (**Fig.**

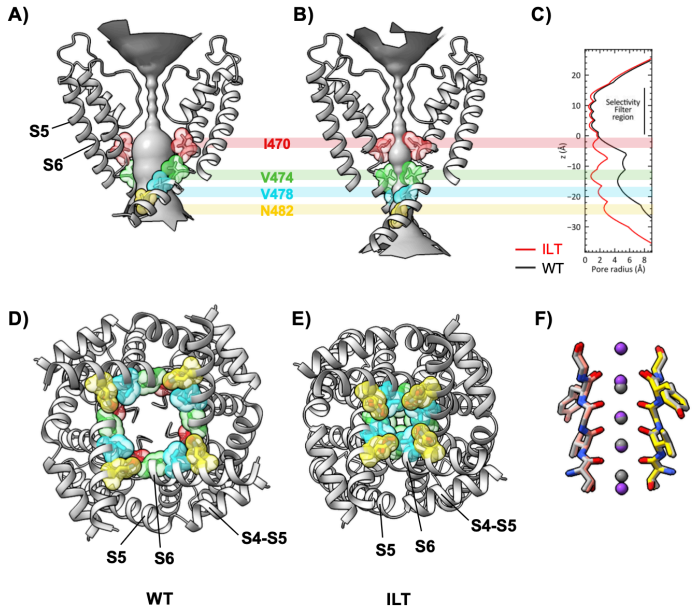

Figure 2. Analysis of the pore domain structure. A) and B) Side view of the WT (left) and ILT (right) pore domain. Four pore lining residues along the S6 helix responsible for constricting the permeation pathway in the ILT structure are highlighted in different colors. D) and E) Bottom view of the intracellular entrance to the permeation pathway showing the open gate for the WT channel and the closed gate for the ILT channel. The four pore lining residues are highlighted in the same colors as in panel A. C) Pore radius for the WT and ILT structures calculated from the HOLE program.[20] F) Overlay of selectivity filter region of WT (Gray) to ILT (colored).

S3), suggesting a possible coupling between these structural elements. The overall differences of Shaker ILT with respect to Shaker WT yield a Cα RMSD of ~2.6 Å.

Compared to the structure of Shaker WT, there are major structural differences consistent with electrophysiology of the ILT mutant (**Fig. 1A**). There is a clear down shift of the S4 helix in the VSD (**Fig. 1C**), accompanied by changes in the position of the S4-S5 linker and the S6 helix of the pore domain (**Fig. 2)**. The lower part of the S6 helix is shifted by ~6 Å towards the center of the pore axis (**Fig. S4)**, starting from Ile468 and gradually increasing to the end of the S6 helix. Importantly, the intracellular gate of the PD appears to be completely closed (**Fig. 2B**, **C, E**), in contrast to Shaker WT (**Fig. 2A**, **D**). The permeation pathway is constricted due to a rotation of the lower half of S6 with respect to the upper half of S6, centered around the second proline (Pro475) in the P-X-P hinge. There are some changes in VDW interactions due to overall movement of the S5 and S6 helices towards the central axis of the pore. Residues Ala463 (chain A) and Thr441 (chain B) as well as Val467 and Thr442 (within the same chain) appear to make a stronger van der Waals contact in ILT compared to WT. The most significant constriction along the pore occurs at residues Ile470, Val474, Val478, and Asn482 (**Fig. 2**). This is confirmed by molecular dynamics (MD) simulation, as water molecules are prevented from entering into the pore (**Fig. S5**). Comparison of pore radius with additional structures are shown in **Fig. S6.** Nonetheless, the selectivity filter of the Shaker ILT structure is in a conductive state with no significant change compared to the Shaker WT structure (**Fig. 2F**). In particular, five K^+ ions can be resolved in the binding sites (based on the sharpened map). The hydrogen bond interaction between Trp434 and Asp447 is intact (**Fig. S7**). In both Shaker WT and Shaker ILT, Trp435 of chain A forms a hydrogen bond with Tyr445 of chain B in the selectivity filter.

Shift of voltage sensor domain (VSD)

The VSD in Shaker ILT displays important differences compared to WT (**Fig. 3A**). The S4 helix is rotated by ~15º and shifted down by ~6 Å (**Fig. 1C** and **Fig. 3B**), consistent with the partial activation observed in electrophysiology (**Fig. 1A**). The downward movement of S4 by approximately one helical turn shifts the interaction pattern of the gating arginine residues within the VSD (**Fig. 1C**). The interactions within the VSD of the WT and ILT structures are summarized in **Table 1**.

The S4 helix in Shaker ILT is stabilized in a different position than in Shaker WT through a number of interactions (**Fig. 3B**). In particular, Phe373 in the S4 helix of subunit A forms a stacking interaction with Phe401 and Phe402 in the S5 helix of subunit C that is not observed in the WT structure (**Fig. S8A**). In particular, the bottom of the ILT S4 helix is shifted towards the S5 helix of the adjacent subunit (**Fig. S8A**) such that ILT-Phe373 (S4) occupies a similar position to WT-Leu382 (S4-S5 linker) and now interacts with Phe401 and Phe402 (S5). Of special importance are the interactions involving the three mutated residues (369, 372, and 376) with the adjacent S5 helix (**Fig. 3B**). In Shaker ILT, Ile369 interacts with Leu409 and

Table 1. Interaction within the VSD

	WT	ILT
R362	Solvent	Solvent
R365	Solvent	E247
R368	E247 (S1)	E283
R371	E283 (S2)	F290
K374	D316 (S3)	E293, D316
R377	D316 (S3)	E218
V363	None	F416
L366	F416	S412, F416, L409
V(I)369	S412	V408, L409
I(L)372	I405, V408, L409	F401, F404, I405
L375	F401, I405	F401
F370	None	L409
F373	L409	F401, F402, I405
S(T)376	L382	L382, F401, F402

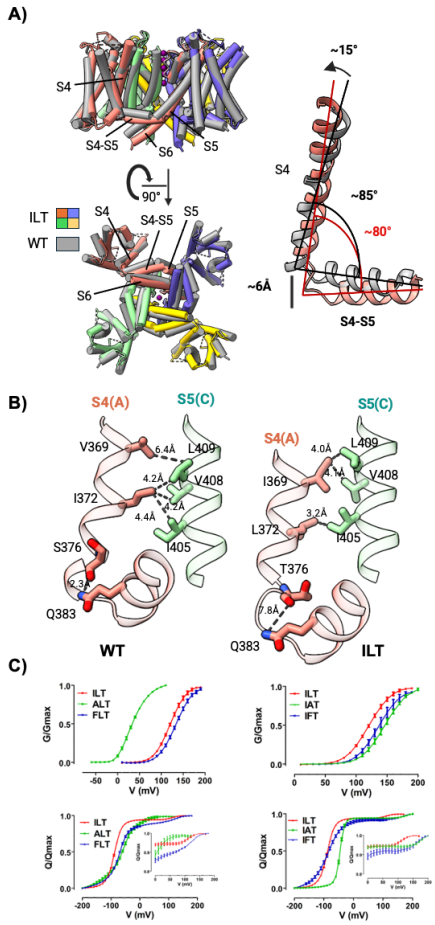

Figure 3. ILT Structure and interactions of ILT residues in the S4 helix: A) Front and bottom view of Shaker ILT structure (each chain shown in different color) superimposed with Shaker WT (gray)**,** the T1 domain is not shown for the sake of clarity. Also shown is the S4 helix translational and angle shift of ~6Å S4-S5 helix vertical down shift in ILT compared to WT. **B)** ILT residues I369, L372 and T376 interact with hydrophobic residues (I405, V408, and L409) in the S5 helix of chain C. **C)** Normalized conductance (G/Gmax)-voltage curve (G-V) and normalized gating current Q/Qmax-voltage curve for ALT and IAT (green), FLT and IFT (blue) and ILT (red).

Val408, while Leu372 interacts with Ile405. However, Thr376 does not appear to form any interaction. In Shaker WT, Val369 interacts with Leu409, while Ile372 interacts with Ile405, Val408, and Leu409. In addition, the backbone carbonyl oxygen of Ser376 forms a hydrogen bond interaction with the side chain of Gln383 in the S4-S5 linker. The average interaction involving the three mutations in the ILT and WT conformational state was calculated from the last 10 ns of a 20 ns (for ILT) and 50 ns (for WT) MD simulation of each conformational state (**Fig. S9**). This simple calculation confirms that the ILT conformation of each VSD is indeed stabilized by about -11 kcal/mol relative to WT in the triple mutant. Specifically, the dominant contribution is made by S376T (-7 kcal/mol), followed by I372L (-5 kcal/mol). To better assess the importance of the various interactions, the effect of substituting a small (Ala) or bulky (Phe) residue at positions 369 and 372 was investigated, yielding the series of Shaker mutants ALT, FLT, IAT, and IFT. The G-V and Q-V curves of the mutants were determined; gating currents were measured using a non-conducting mutant (W434F), which was also used to characterize Shaker WT and ILT. Comparing the G-V curves of the residue 369 mutants to that of ILT, ALT becomes conductive at a lower voltage, displaying a -90 mV shift in G-V while FLT shows a +10 mV shift (Fig. 3C). In the Q-V curves both mutants are shifted +10 mV but the biphasic component observed in ILT does not appear for ALT but is increased for FLT. This observation suggests that the size of the residue in position 369 affects the

stability of the ILT intermediate conformational state captured by the original ILT mutant. The G-V curves for the residue 372 mutants compared with ILT, IAT and IFT show a +25 mV and +15 mV shift respectively (Fig. 3C). Their Q-V curves show a +30 mV shift for IAT and a 0 mv shift for IFT, and both curves display the biphasic component. To better interpret these results, the Q-V curves were fitted with gating charge calculated from MD simulations (see **Fig. S13** and text below).

S4-S5 linker shift related to VSD and interaction with intracellular gate

In the Shaker ILT structure, there is a downward displacement of the S4-S5 linker by ~6 Å and an inward displacement of S6 by ~6 Å towards the center of the pore axis compared to Shaker WT (**Fig. S4**). Remarkably, despite the differences with the open or closed gate of the WT and ILT structures, most of the main interactions involving the S4-S5 linker, the S5, and S6 helices are conserved (though there are small shifts in side-chain configurations). Each S4-S5 linker is interacting simultaneously with two S6 helices (**Fig. S4** and **Fig. S8**). Important interactions between the S4-S5 linker and the S6 helix within the same subunit include residues Ile384 and Thr388 with Phe481, Phe484, and Tyr485 (**Fig. S4**). Additional interactions across different subunits include residues Leu382 and Leu385 in the S4-S5 linker of subunit A with Phe401 and Phe402 in the S5 helix of subunit C (**Fig. S8A**), Ser479 and Asn480 in the S6 helix of subunit A with Asn482 and Tyr485 (**Fig. S8B**), Arg394 and Glu395 of the S4-S5 linker of subunit A with Tyr485 in the S6 helix from subunit B (**Fig. S7C**), and finally, Leu398 and Phe402 in the lower part of the S5 helix in subunit A with Phe481 of the S6 helix from subunit B (**Fig. S8D**). All cross-subunit interactions are reproduced clockwise in the tetramer.

Structure based AlphaFold selection and MD simulation

To achieve a more complete perspective of the full activation cycle, the structure of Shaker ILT was used as a template to generate models of additional intermediate states with AlphaFold2 combined with MD simulations (**Fig. S10)**. It is known that the VSD can adopt a few discrete conformations {Li, 2014 #334;Shen, 2022 #333}. Those conformation can be conveniently identified based on the number of gating charges along the S4 helix crossing the hydrophobic region formed by residues Phe290 and Ile287 [21,22], referred to as "click". This yields a total of five states for the VSD: up, 1-click down, 2-clicks down, 3-clicks down, and 4-click down. The VSD in the ILT intermediate structure corresponds to 1-click down from the WT up state (0-click), used as a reference. A number of models generated by AlphaFold produced conformations with a VSD that is 2-clicks down relative to the WT structure (**Fig. S11**). Following critical evaluation, no additional conformations of the VSD could be generated. Two additional conformations were generated from this model using MD simulations with an applied membrane potential. A simulation at -400 mV produced a conformation with a VSD that is 3-clicks down relative to the WT structure, and -a simulation at -750 mV produced a conformation with a VSD that is 4-clicks down relative to the WT structure. Combining these MD conformations with the two experimental structures (WT and ILT) and the AlphaFold model, yields a total of five conformational states of the VSD. Counting the gating charges starting from the Up state, the conformational transitions of the VSD can be described as 1-, 2-, 3-, or 4-clicks down. The ILT conformation is 1-click down. For the sake of simplicity, the VSD conformation in the WT structure is said to be in the "Up" state (0-click down), and the 4-clicks down model is said to be in the "Down" **(Fig. 4A)**. Features of the different VSD conformations are characterized in **Fig. S12**.

To explore the detail of the final stages preceding the opening of the gate after complete voltage activation, one additional conformational state of the channel was generated between the ILT and WT conformations. This corresponds to a fully activated VSD (as in Shaker WT) and a PD with a closed gate (as in Shaker ILT). The model was obtained from a targeted MD (TMD) simulation started from Shaker-ILT (reverted to WT sequence) using the activated VSD S4 of Shaker WT as a target. The TMD forces applied only to the S4 helix targeting the position of the Up state of the VSD without restraint on the remaining residues

(including the S4-S5 linker). During this Targeted MD (TMD), the S4-S5 linkers can either remain in contact with the closed gate or move to the activated position of the activated state. However, during an unbiased MD simulation of almost 10 µs, two out of four S4-S5 linkers spontaneously make a transition from the locked position associated with the closed gate to the activated position that they occupy in the WT activated conformation (**Fig. S14** and **Movie S1)**. The two other linkers dissociate from the gate and become more labile, partly losing their helical structure. It is expected that, in time, all four S4-S5 linkers shall adopt the activated conformation while the intracellular gate remains closed.

In total, we have six conformational states of the channel, labeled *i* to *vi*, mapping the activation process (**Movie S2).** Analysis of MD trajectories shows that Leu370 is more exposed to water molecules in the resting state but is inserted into a nonpolar pocket in the activated state, consistent with the experimental finding that the leucine sidechain either stabilizes the resting state or destabilizes the activated state [26,27]. The conformational change mapped through the sequence of six states correlates well with experimental data showing that substitution of Leu382 (named 370) in the S4-S5 linker by a polar residue should shift the voltage-activation to higher voltages [26,27]. Furthermore, the gating charges of the individual activation steps of the channel calculated from MD simulations increase from 0 to 14.5 *e* (**Fig. 4B**) yielding families of Q-V curves that are in accord with electrophysiology measurements for WT as well as a series of mutants

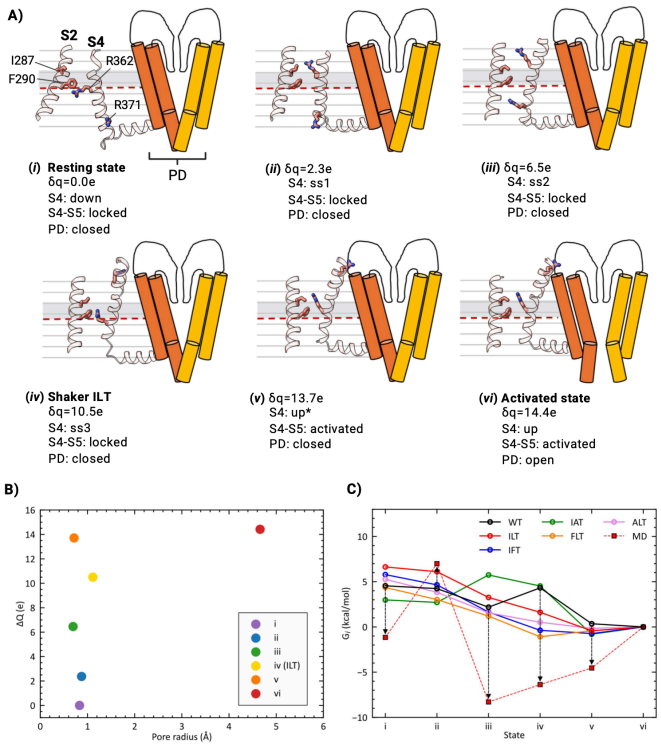

Figure 4. Conformational steps along the voltage activation process. A) The channel conformation is summarized in terms of 3 structural features: the gate of the PD, the VSD, and the S4-S5 linker. The intracellular gate of the PD can be either closed (as in ILT) or open (as in WT); the VSD can be in the state down or 4CD, 3CD, 2CD, 1CD (as in ILT), and 0CD or "up" (as in WT); the S4-S5 linker can be locked (as in ILT), activated (as in WT), or locked (as in ILT). The six conformations along the voltage activation process are (**i-vi**): closed-down-locked (δq=0.0*e*), closed-3CD-locked (δq=2.3*e*), closed-2CD-locked(δq=6.5*e*), the ILT mutant channel closed-1CD-locked (δq=10.5*e*), closed-up-locked (δq=13.7*e*), and the WT channel open-up-activated (δq=14.4*e*). During the transitioning from state *iv* to state *v*, the S4-S5 linker is observed to be in a dynamical labile state, fluctuating between keeping in contact with the S5-S6 gate, or moving up toward the activated position observed in state *v* and state *vi* (the WT structure). **B)** Relation between the gating charge (ΔQ) and the opening of the most constriction point along the pore radius at Val474. **C)** Relative free energy at zero membrane potential from Q-V curve fitting obtained from Scheme 1 for the different mutants using the ΔQ of states *i* to *vi* and compared with the interaction estimated from MD simulations of WT and ILT mutant in the conformations of states *i* to *vi* (**Figs. S9** and **S13**).

(**Fig. 3C** and **Fig. S13**). Interestingly, S4 adopts a standard α-helical conformation in the early states *i* to *iii* that progressively becomes a 3_{10} helical conformation in response to membrane depolarization beginning at state *iii* (**Fig. S12D**).

DISCUSSION

The Shaker ILT mutant provided a unique opportunity to capture a Kv channel in a previously unobserved conformation as determined from single particle CryoEM (**Fig. 1B**). In this novel conformation the intracellular gate of the PD is in a tightly closed non-conducting state. Furthermore, the position of the S4 helix in the VSD is shifted down by ~5 Å relative to the fully activated and open state of the WT channel structure (**Fig. 1C**). The VSD and the S4 helix are stabilized in this intermediate position by specific interactions involving a residue of the ILT mutation (Ile369) and Val408 and Leu409 in the S5 helix of the PD (**Fig. 3B**). Examination of the pore radius of the closed state reveals the importance of two separate gates along the permeation pathway: an innermost gate formed by residues Ile470 and Val474 in the S6 helix closer to the selectivity filter, and a second gate formed by residues Val478 and Asn482 near the intracellular side **(Fig. 2**). Studies of the Kv1.2-2.1 chimera channel previously indicated that a constriction of the pore at the level of residue I398 corresponding to I470 in Shaker was also involved in C-type inactivation [23,24]. Interactions of the S4-S5 linker with S6 involving nonpolar sidechains (Ile384 and Thr388 with Phe481, Phe484 and Tyr485) also help to stabilize the closed conformation of the PD (**Fig. S4C** and **D**). Interestingly, the same interactions are also observed in the open state despite the conformational shift of ~6 Å. This shows that the interface formed by the S4-S5 linker with S6 exists in conformations with both open and closed gates.

The present results, combining cryoEM (**Figs. 1-4**), electrophysiology (**Fig. 3D**), structural modeling (**Fig. S10**), MD calculations (**Fig. S12**), and kinetic modeling (**Fig. S13**), provide the crucial information to help understand the voltage gating process. The two CryoEM structures together with the four computational models yield a total of six conformations of Shaker mapping the complete sequence of states along the voltage activation process, starting from the closed resting state *i* to the activated open state *vi* (**Fig. 4A** and **Movie S2**). One can describe these six states by focusing on 3 main structural elements: the gate of the PD, the VSD, and the S4-S5 linker. The gate can be closed or open, the VSD can adopt five different conformations (0- to 4-clicks down from the WT up state), and the S4-S5 linker can be either activated (as in WT) or locked (as in ILT). The incremental gating charge of the six states along the voltage activation pathway was calculated using MD simulations. Starting from the resting to the activated state, the values are 0.0, 2.3, 6.5, 10.5,13.7, and 14.4*e*. The latter matches well the experimentally observed gating charge of Shaker [28-30]. In addition, those incremental gating charges can be used to reproduce the measured Q-V of Shaker and several mutants (**Fig. 4B**). The best fit to the experimentally measured Q-V curve is obtained with a model treating the four VSD independently, with a single cooperative step from the state *v* to *vi*, the activated open state, in accord with previous kinetic modeling of Shaker voltage-activation[31-33] (**Fig. S13**). This consistent with the electrophysiology data indicating that this final transition is cooperative [31-33], and the fact that each S4-S5 linker is simultaneously contacting two S6 segments (**Fig. S4** and **Fig. S8**).

Having validated the structural models of the states along the voltage gating process, it is now possible to try to explain the structural basis of the E-M coupling governing the activation of Kv channels (**Fig. 4A** and **Movie S2**). Under a large negative potential, the state *i* is dominant and the gate is closed. This is the resting state of the Kv. Membrane depolarization promotes the transition of the VSD to the up state. The experimental structures complemented by the computational modeling indicate that the membrane depolarization drives the conformational change of the VSD through a sequence of states (**Fig. 4B**). The conformational change of the VSD through this sequence of steps is strongly voltage-dependent with a total incremental charge of 13.7*e*. However, despite the voltage-driven conformational change within the VSD,

the S4-S5 linker remains in its locked position and the gate remains closed in states *ii*, *iii*, and *iv* (the conformation revealed by the cryo-EM structure of the Shaker ILT triple mutant). Even the subsequent transition from state *iv* to state *v*, in which the VSD goes from 1-click down to up, does not cause the opening of the gate. In state *v* that all four S4-S5 linkers are disengaged from the S5-S6 gate to adopt the activated position seen in the WT structure. The linkers are positioned to stabilize the open gate, which remains closed. In state *v*, the closed gate corresponds to a metastable conformation with a finite lifetime, ready to makes a spontaneous transition to the open conformation. This final transition from state *v* to state *vi* is only weakly voltage-dependent, with a small incremental charge of only ~0.7*e* because it is associated with a focusing of the membrane electric field along the permeation pore—a scenario that is consistent with previous analysis of Shaker gating [31-33]. The striking functional phenotype of Shaker ILT mutant is caused by the stabilization of the intermediate conformational state *iv* relative to Shaker WT. This intermediate conformational state *iv* (**Fig. 4A**) has the VSD almost fully activated but the S4-S5 linker keeping the intracellular gate closed. Consequently, the stepwise voltage-activation process of Shaker ILT "stalls" in the intermediate state *v* even though the Q-V has almost reached its maximum while the G-V is still zero. Although the functional phenotype of Shaker ILT has traditionally been interpreted from the assumption that the mutations in the S4 helix decouples the movement of the VSD from the gate opening [14-16], the structural coupling between the VSD, the S4-S5 linker, and the intracellular gate is completely unaffected by the triple mutation.

In final analysis it is important to note that through the sequential step of voltage activation, the vertical movement of the sliding S4 helix is not mechanically "pulling" on S5 and S6 via the linker to "pry" the gate open. Rather, the voltage-driven conformational transition of S4 within the VSD transforms the environment that stabilized the S4-S5 linker in contact with the closed gate. The penultimate state preceding activation with the linker in its activated position creates an alternative environment that stabilizes the open gate through an equilibrium shift mechanism. As revealed by the details of the final steps from state *iv* (ILT structure), *v*, and *vi* (WT structure), the nature of the E-M coupling that opens the gate of the channel results from a dynamic shift in population equilibrium between metastable states.

ACKNOWLEDGEMENT

The authors are grateful to the staff of the single particle CryoEM facility at The University of Chicago for their assistance during sample screening and data collection. The help of Patrick Haller is gratefully acknowledged. This work was supported by NIH grant 5R35GM152124, and by computational resources provided by the Research Computing Center of The University of Chicago and the Beagle3 high-performance GPU cluster funded by the NIH through grant 1S10OD028655.

MATERIALS AND METHODS

Site directed mutagenesis and cloning. To generate the Shaker ILT construct, the mutations of V369I, I372L, and S376T were introduced by a modified QuikChange site-directed mutagenesis protocol [34] into the Shaker zH4 K+ channel with removed N-type inactivation (IR, Δ6-46) [35] in the pBSTA vector used for electrophysiological experiments. Additional mutations W434F were introduced on top of Shaker V369I/I372L/S376T (ILT) in pBSTA to record gating current [29]. Other mutations (ALT, FLT, IAT, IFT) were generated for functional studies to measure gating and ionic current. For structural studies, Shaker ILT was cloned into the 5' EcoRI and 3' XbaI sites of a modified pEG BacMam vector containing a C-terminal HRV 3C protease site, an eGFP tag and an 8× His tag. All plasmid constructs used for expression were checked by either Sanger (University of Chicago DNA Sequencing Core Facility) or nanopore (Plasmidsaurus) sequencing to confirm the desired mutations.

Cell lines. The HEK293S GnTI- cells in suspension that were used for protein expression and purification were obtained from ATCC (CRL-3022). GnTI- cells were grown at 37 °C and 7.8% CO_2 in FreeStyle 293 expression medium (Gibco, Thermo Fisher Scientific) supplemented with 2% heat-inactivated fetal bovine serum (FBS) and 10 μg ml^{-1} penicillin–streptomycin. Sf9 cells (Thermo Fisher Scientific, 12659017) were cultured in SF-900 II SFM medium (Gibco, Thermo Fisher Scientific) supplemented with 10% FBS and 10 μg ml−1 gentamicin at 28 °C.

Expression and purification of Shaker ILT. To obtain a biochemically stable preparation suitable for single-particle cryo-electron microscopy (CryoEM), the Shaker ILT protein was expressed in HEK293S GNTI- cells (ATCC). The pEG BacMam/Shaker ILT plasmid and the Bac-to-Bac system (Invitrogen) were used to generate a recombinant bacmid. Sf9 insect cells (Thermo Fisher Scientific) were transfected with the bacmid using Cellfectin II (Thermo Fisher Scientific) to generate P0 baculovirus. After amplification, the P1 baculovirus was used to transduce HEK293S GNTI- cells at a ratio of 1:10 (v/v). After 20–24 h of incubation at 37 °C, 10 mM sodium butyrate was added to the cells and the culture was transferred to 30 °C. Cells were collected 54–58 h after transduction by low-speed centrifugation. The cell pellets were washed with phosphate-buffered saline pH 7.4, collected by low-speed centrifugation, flash-frozen and stored at −80 °C for later purification. Purification was carried out on ice or at 4 °C. The flash-frozen cell pellets (0.5 l) were thawed in a water bath at room temperature and Dounce homogenized in the presence of 50mM Tris-Cl pH 7.5, 150mM KCl buffer, 2mM TECP (Buffer A) containing 10 μg ml−1 DNase and a complete Protease Inhibitor Cocktail (Roche). Protein was extracted with a 1.5% n-dodecyl-β-d-maltopyranoside (DDM; Anatrace) and 0.15% cholesteryl hemisuccinate (Anatrace) for 120 min. Solubilized supernatant was isolated by ultracentrifugation at 100,000xg RPM, 1h, 4°C. The supernatant was incubated for 2 h with 2 ml CNBR-activated Sepharose beads (GE Healthcare) coupled with 4 mg high-affinity GFP nanobodies. The beads were transferred to a plastic column and further washed with 10 column volumes of buffer A containing 0.05% DDM (Anatrace) and 0.01% cholesteryl hemisuccinate, exchanging stepwise to buffer A containing 0.02% GDN. Protein was cleaved by HRV 3C protease overnight at 4 °C, concentrated and analysed using SEC on a Superose 6, 10/300 GE column (GE Healthcare) in buffer A with 0.02% GDN. Peak fractions were collected and concentrated using a 100 kDa molecular mass cut-off centrifugal filter (Millipore) to ~1 mg ml^{-1}. The concentrated protein was used immediately for cryo-EM.

Cryo-EM sample preparation and data acquisition. UltrAufoil 300-mesh 1.2/1.3 Au grids (Quantifoil) were plasma-cleaned at 20W for 40 s in an air mixture in a Solarus Plasma Cleaner (Gatan). Purified Shaker ILT samples were applied to the grids and frozen in liquid-nitrogen-cooled liquid ethane using a Vitrobot Mark IV (FEI) and the following parameters: 3.5 µl sample volume; 3.5 s blot time; 1.0 blot force; 100% humidity; temperature of RT. Grids were screened for single particles on a 200kV Glacios TEM with cryo-autoloader equipped with a K2 summit direct detector (Gatan). Grids were imaged at the University of Chicago on a Titan Krios with a K3 detector and GIF energy filter (set to 20 eV) at a nominal magnification of ×81,000, corresponding to physical pixel size of 1.068 Å. Movies were acquired for 50 frames with total exposure 60 e^{-} A^{-2}.

Single-particle cryo-EM analysis. All steps for structure determination were performed using CryoSPARC [36], including motion correction and contrast transfer function (CTF) estimation. A dataset of ~6600 movies was collected, and particles were picked and classified in 2D to generate templates for template-based particle picking. Approximately 2.6 million initial particles were picked and subjected to 2 rounds of 2D classification. From these, 0.45 million particles were selected to generate two *ab initio* models for C1 and C4 symmetry separately. This process was repeated multiple times to eliminate junk particles. ~0.29 million particles from the best class were processed for 3D refinement (non-uniform or local refinement) with the C4 refinement algorithm [37], which consistently yields the best results. Reference-Based Motion correction was applied to estimate per-particle movement trajectories and empirical dose weights. These particles

underwent a further 3D refinement step, followed by local refinement using a mask with enforced C4 symmetry. Local resolution was calculated using CryoSPARC.

Model building, refinement and molecular visualization. The Shaker-IR WT structure (PDB ID: 7SIP) was used as a template to build atomic models for Shaker ILT. Secondary structural elements were fit into the map and further model building was pursued through iterative rounds of manual model building in COOT [38] registering secondary structural elements using bulky residues such as Phe and Arg. Simultaneously, flexible loops fitting in position in the atomic models were obtained using interactive flexible fitting in ISOLDE [39]. The density was of sufficient quality to assign rotamers for key residues whereas side chains of some residues that could not be assigned even tentative rotamers were truncated at the Cβ position of the residue. The tetramer model was generated by applying C4 symmetry operations to the monomer in UCSF ChimeraX [40,41]. Models were refined iteratively using phenix.real_space_refine in Phenix [42]. PDB validation has been performed in the PDB validation server. All structural analyses and figure generation were performed using UCSF ChimeraX.

Electrophysiological recordings and analysis. *Xenopus laevis* ovaries were obtained from Xenopus 1 (Dexter, Michigan). The follicular membrane was digested by collagenase 2 mg/mL supplemented with bovine serum albumin 1mg/mL. Oocytes were kept at 12 or 18 ºC in SOS solution containing (in mM) 96 NaCl, 2 KCl, 1 $MgCl_2$, 1.8 $CaCl_2$, 10 HEPES, pH 7.4 (NaOH) supplemented with gentamicin (50 mg/ml). We used clones of the Shaker zH4 K^+ channel with removed N-type inactivation (IR, Δ6-46) in the pBSTA vector [35]. pBSTA Shaker DNA was linearized using NotI enzyme and cRNA was transcribed using the T7 RNA kit (Invitrogen T7 Transcription Kit). cRNA was injected in defolliculated oocytes (stage V-VI) and incubated in SOS solution at 18 or 12 ºC. After 1-4 days currents were recorded using the cut-open voltage-clamp method [43]. Voltage-sensing pipettes were pulled using a horizontal puller (P-87 Model, Sutter Instruments, Novato, CA). The resistance ranged between 0.2-0.5 MΩ. Data were filtered online at 20–50 kHz using a built-in low-pass four-pole Bessel filter in the voltage clamp amplifier (CA-1B, Dagan Corporation, Minneapolis, MN, USA) sampled at 1 MHz, digitized at 16-bits and digitally filtered at Nyquist frequency (USB-1604; Measurement Computing, Norton, MA) using Gpatch64M (in-house software). An in-house software (Analysis) was used to acquire and analyze the data. External solution for ionic recording was composed of (mM): K-Methanosulfonate (MES) 12, N-Methyl D-glucamine (NMG)-MES 108, Ca-MES 2, HEPES 10, pH 7.4, and internal solution of (mM): K-MES 120, EGTA 2mM, HEPES 10, pH7.4. For right shifted mutants the external solution contained K-MES 120, Ca-MES 2, HEPES 10. External solution for gating currents recording was composed of (mM): NMG-MES 120, Ba-MES 2, HEPES 10, pH 7.4, and internal solution of (mM): NMG-MES 120, EGTA 2mM, HEPES 10, pH 7. The ionic current was measured when the current reached a steady-state level and then converted to conductance (G) using the equation, $G = I/[V - (RT/F)\ln([K^+]_{\mathrm{out}}/[K^+]_{\mathrm{in}})]$, where I is the current, V is the membrane voltage, R is the gas constant, T is the temperature in Kelvin, F is the Faraday constant, and $[K^+]_{in}$ and $[K^+]_{out}$ are the intracellular and extracellular K^+ concentrations, respectively. The individual K^+ conductances were then normalized, averaged, and plotted against V to build conductance-voltage (G-V) curves. The data was fitted using two-state and three-state models [19].

AlphaFold structure predictions. Structural models of the Shaker tetramer (residues 206-491) were generated using AlphaFold2[[4445] through ColabDesign v1.2.0b3[[46,47]]. The coordinates of the S1/S5/S6 helices of the Shaker-ILT tetramer in the intermediate gate-closed conformation were used as the only structural template and initial guess. MSAs were generated for the VSD + S4-S5 linker (residue 206-397) in either WT or ILT sequences using the ColabFold 1.5.5 API and the AF-Cluster [48]. MSA reduction method was used to cluster the MSA (39 clusters for WT, 32 clusters for ILT) to prompt exploration of alternative VSD conformations. Each MSA sequence was then recombined with the pore-domain sequence into a full-length sequence. Each MSA cluster and the pore-domain template was then input into AlphaFold, generating a structure for each cluster and each of the 5 AlphaFold2 multimer_v3 models. Each structure

was recycled a maximum of 20 times, using the coordinates of the previous cycle, an early stop tolerance of 0.5 Å RMSD between cycles, and with no activation of dropout layers. Misfolded structures were filtered out and the remaining 312 out of 355 structures were then classified into 0, 1, or 2 click-down states by whether the sidechain of each S4-helix Arg residues was below the hydrophobic plug formed by residue F290 and I287. Of 7 structures categorized as 2-click down, 1 had an S4 shifted down by a full turn and was selected for MD simulations as described below.

MD simulations. Atomic models for the Shaker channel in various conformational states were constructed using residues 206 to 491 for MD simulations. The simulations were performed with OpenMM 8.1.2 [49]. The CHARMM force field CHARMM36m[50] for protein [51-54], lipids[55], ions[56], and TIP3P[57] was used. The default parameters from the CHARMM-GUI input files were used except a switching function was used to smoothly truncate the potential at the cutoff beginning at 10 Å. The temperature was held constant at 310 K. Constant pressure simulations were performed at 1 atm. An initial system containing the Shaker channel was first prepared using the CHARMM-GUI membrane builder,[58-61] which is inserted in a bilayer of POPC (1-palmitoyl-2-oleoyl-phosphatidylcholine) lipids and solvated in 150 mM KCl, and with all sidechains being assigned their standard protonation state. Subsequently, the channel can then be swapped with its other conformational states. In all cases the selectivity filter was initially loaded with K^+ ions at binding sites S_0, S_2, and S_4,[62] with water occupying the intervening sites.

Simulations were conducted at a 2 fs timestep and with a force constant of 1 kcal/mol/Å^2 for positional restraints, except when stated otherwise. Equilibration was generally performed in 3 steps, with changes noted below. In all steps the loops of the VSD (at the level of Thr265 and Ala343 Cα atoms) were held packed in a 50 Å radius cylinder centered on the channel to prevent the full extension of the loops in the xy-plane. The 1st equilibration step was performed with positional restraints on all protein residues, excluding those that are unresolved in the cryo-EM structure, and a flat-bottom restraint applied to the oxygen of water molecules to prevent them from entering the membrane region. The system was energy minimized for 400 steps and then equilibrated for 100 ps at NVT (constant Number of particles, Volume, and Temperature) conditions, followed by 10 ns at NPT (constant Number of particles, Pressure, and Temperature) conditions. A 2nd equilibration step was performed without the water restraints for 20 ns or until the box-volume converged, taking at least 90 ns but no more than 130 ns. After this step, the channel is reverted/mutated to a common sequence, in either WT or ILT, and the gating charge is determined as detailed below. Next, the 3rd equilibration step was performed for 10 ns with protein restraints reduced to backbone restraints on all TM helices, S4-S5 linker, pore helix, and selectivity filter. Production simulations were then performed for 1.2 μs with a center of mass (COM) positional restraint on Val467 Cα atoms to prevent the channel from drifting. The trajectories were analyzed with VMD [63] and the first 200 ns were omitted from the analysis.

For the simulations based on the cryo-EM structures, the protein was restrained during the 1st equilibration step with a force constant of 100 kcal/mol/Å^2. The 3rd step was performed for 11 ns with the 100 kcal/mol/Å^2 position restraint being linearly scaled off over the last 10 ns. The state *ii* conformation in WT sequence was only equilibrated following the 1st step, and with only the Cα atoms restrained.

A model of Shaker WT with a closed gate (as in ILT) and activated VSD (as in WT) was generated to explore the final stages of gate opening after voltage activation using targeted MD. The TMD is started from Shaker ILT reverted to WT after the 2nd equilibration step and the activated VSD S4 of 7SIP is used as a target. After reverting the mutant, the system was first energy minimized for 200 steps, and equilibrated for 50 ns at NPT conditions with the backbone restrained. The activated VSD S4 was then targeted starting at a 1 kcal/mol/Å^2 restraint that was linearly increased to 100 kcal/mol/Å^2 over 11 ns while the remaining residues (including the S4-S5 linker) were left free. This was then equilibrated for 10 ns with only the S4

helix backbone restrained at 1 kcal/mol/Å^2. A production simulation was then taken to 10 µs with the S4 released.

Transmembrane potential simulations. A model for the resting state of Shaker, closed gate and VSD down, was explored with a transmembrane potential at hyperpolarizing voltages, which was implemented with an electric field [64]. The Shaker ILT in ILT and WT sequence and the Shaker WT AlphaFold2 model were each considered at -400 and -750 mV. All systems were initialized after the equilibrations described above plus an added 100 ns equilibration at NPT conditions with backbone restraints on the PD, secondary structure restraints on the S4-S5 linker, and the initial loading state of the selectivity filter held fixed with position restraints on the K^+ ions. The VSD was left free to move. Afterwards the membrane potential at -400 or -750 mV was introduced at NVT conditions. The first 200 ns were done at 2 fs, which was then increased to 4 fs after hydrogen mass repartitioning, the hydrogen mass was increased threefold. The simulations at -400 mV were sampled for 6 µs and simulations at -750 mV for 3 µs. A subunit was observed to transition to state *ii* for the ILT sequence after 1.6 µs at -750 mV, and for the AlphaFold2 model after 400 ns at -400 mV and to state *i* after 2 µs at -750 mV. To assess the reliability of the obtained conformation of state *i* from the AlphaFold2 model at -750 mV an initial equilibration was performed at NPT conditions without voltage for 200 ns. Next, a TMD step is used to obtain the final model because all VSDs act independently of the others so not all subunits complete the transition; thus, in the TMD the VSD and S4-S5 linker residues of the subunit that completed the transition is used as a target to the remaining subunits. The PD was restrained in the closed gate conformation in this TMD step. The TMD restraint began at 1 kcal/mol/Å^2 and is linearly increased to 100 kcal/mol/Å^2 over 11 ns at NPT conditions. The channel was then symmetrized in vacuum for 55 ns at NVE (constant Number of particles, Volume, and Energy) conditions with the Verlet integrator at a 1 fs timestep. The symmetry restraint began at 1 kcal/mol/Å^2 and was linearly increased to 100 kcal/mol/Å^2 in the first 11 ns. The final model was acquired after 2,000 steps of minimization with the symmetry restraint increased by four-fold. The final models were then assessed with production simulation as described above.

Gating charge calculation. The gating charge of Shaker in the six conformational states was calculated using MD simulations via the average displacement charge at zero membrane potential according to the Q-route theory [64,65]. After the 2nd equilibration step, each state was then mutated to a common sequence (WT or ILT). The channels requiring a mutation were first energy minimized for 200 steps. The simulations to calculate the gating charge were performed at NPT conditions with backbone restraints on all resolved residues and the initial occupancy of the selectivity filter held fixed with restraints on the K^+ ions z-position. Three replicates were performed for each state; WT sequences were simulated for 50 ns and ILT sequences for 20 ns. The gating charge was then estimated from the displacement charge, omitting the first 10 ns from the calculation [64,65].The experimental activation curve Q-V was fitted using the estimated gating charge transfer of the states. The activation process is represented according to Scheme 1,

Scheme 1

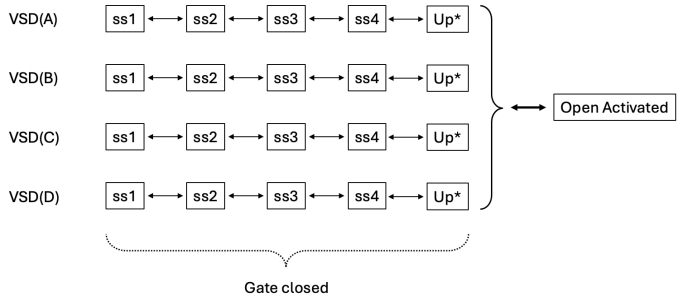

which involves independent transitions of the four VSD through five states with the gate closed before a final cooperative transition to the open activated state. The equation for the total gating charge Q as a function of voltage V follows,

$$Q(V) = \frac{1}{S}\sum_{a=1}^{5}\sum_{b=1}^{5}\sum_{c=1}^{5}\sum_{d=1}^{5} Q(a,b,c,d)e^{-\left(\left(G(a)+G(b)+G(c)+G(d)\right)-Q(a,b,c,d)V\right)/k_{\mathrm{B}}T} + Q_{vi}e^{-(G_{vi}-Q_{vi}V)/k_{\mathrm{B}}T}$$

where Q_{vi} is the incremental charge of the state *vi* (open activated), and the index *a, b, c, d* denote the states of each of the four VSD, yielding the incremental charge

$$Q(a,b,c,d) = \delta q(a)/4 + \delta q(b)/4 + \delta q(c)/4 + \delta q(d)/4$$

with the normalization constant,

$$S = \sum_{a=1}^{5}\sum_{b=1}^{5}\sum_{c=1}^{5}\sum_{d=1}^{5} e^{-\left(\left(G(a)+G(b)+G(c)+G(d)\right)-Q(a,b,c,d)V\right)/k_{\mathrm{B}}T} + e^{-(G_{vi}-Q_{vi}V)/k_{\mathrm{B}}T}$$

The Q-V curves are normalized to 1 at large voltage. This scheme is reminiscent of a combination of class B and D kinetic models proposed in Zagotta et al. 1994, which states that each subunit must undergo four conformational changes at the VSD before opening with a final concerted opening of the gate{Hoshi, 1994 #340}. The free energy of each closed state was fitted relative to the free energy of the activated state (fixed to zero). The gating charge estimates from the MD simulations and their uncertainty were used in the fitting. The results are shown in **Fig. S13**.

REFERENCES

1. M. F. Schneider & W. K. Chandler. Voltage Dependent Charge Movement in Skeletal Muscle: a Possible Step in Excitation-Contraction Coupling. 187-187 (Eighth Inter. Sedim. Congress, 1972).
2. C. González, D. Baez-Nieto, I. Valencia, I. Oyarzún, P. Rojas, D. Naranjo & R. Latorre. K+ channels: Function-structural overview, *Comprehensive Physiology* **2**, 2087-2149 (2012).
3. A. V. Grizel, G. S. Glukhov & O. S. Sokolova. Mechanisms of Activation of Voltage-Gated Potassium Channels. 2014-2014 (2014).
4. R. Blunck & Z. Batulan. Mechanism of electromechanical coupling in voltage-gated potassium channels, *Frontiers in Pharmacology* **3 SEP** (2012).
5. M. Jensen, V. Jogini, D. W. Borhani, A. E. Leffler, R. O. Dror & D. E. Shaw. Mechanism of voltage gating in potassium channels, *Science* **336**, 229-233 (2012).
6. D. S. D. M. P. Sang-Ah Seoh & B. Francisco. Voltage-Sensing Residues in the S2 and S4 Segments of the Shaker K Channel. (1996).
7. E. Vargas, V. Yarov-Yarovoy, F. Khalili-Araghi, W. A. Catterall, M. L. Klein, M. Tarek, E. Lindahl, K. Schulten, E. Perozo, F. Bezanilla & B. Roux. An emerging consensus on voltage-dependent gating from computational modeling and molecular dynamics simulations, *J. Gen. Physiol.* **140**, 587-594 (2012).
8. R. Shen, Y. Meng, B. Roux & E. Perozo. Mechanism of voltage gating in the voltage-sensing phosphatase Ci-VSP, *Proc Natl Acad Sci U S A* **119**, e2206649119 (2022).
9. S. C. Guo, R. Shen, B. Roux & A. R. Dinner. Dynamics of activation in the voltage-sensing domain of Ciona intestinalis phosphatase Ci-VSP, *Nat Commun* **15**, 1408 (2024).
10. X.-F. Tan, C. Bae, R. Stix, A. I. Fernández-Mariño, K. Huffer, T.-H. Chang, J. Jiang, J. D. Faraldo-Gómez & K. J. Swartz. Structure of the Shaker Kv channel and mechanism of slow C-type inactivation. 7814-7814 (2022).

11. W. Ye, H. Zhao, Y. Dai, Y. Wang, Y. h. Lo, L. Y. Jan & C. H. Lee. Activation and closed-state inactivation mechanisms of the human voltage-gated KV4 channel complexes, *Molecular Cell* **82**, 2427-2442.e2424 (2022).
12. V. S. Mandala & R. MacKinnon. Electric field–induced pore constriction in the human Kv2.1 channel, *Proceedings of the National Academy of Sciences of the United States of America* **122** (2025).
13. Y. Liu, C. Bassetto, G. Contreras, E. Perozo & F. Bezanilla. (2025).
14. C. J. Smith-Maxwell, J. L. Ledwell & R. W. Aldrich. Uncharged S4 Residues and Cooperativity in Voltage-dependent Potassium Channel Activation. 421-439 (Aggarwal and MacKinnon, 1998).
15. J. L. Ledwell & R. W. Aldrich. Mutations in the S4 Region Isolate the Final Voltage-dependent Cooperative Step in Potassium Channel Activation. 389-414 (Sigg and Bezanilla, 1999).
16. M. Pathak, L. Kurtz, F. Tombola & E. Isacoff. The cooperative voltage sensor motion that gates a potassium channel, *Journal of General Physiology* **125**, 57-69 (2005).
17. S. K. Upadhyay, P. Nagarajan & M. K. Mathew. Potassium channel opening: A subtle two-step, *Journal of Physiology* **587**, 3851-3868 (2009).
18. A. I. Fernández-Mariño, T. J. Harpole, K. Oelstrom, L. Delemotte & B. Chanda. Gating interaction maps reveal a noncanonical electromechanical coupling mode in the Shaker K+ channel, *Nature Structural and Molecular Biology* **25**, 320-326 (2018).
19. J. J. Lacroix, S. A. Pless, L. Maragliano, F. V. Campos, J. D. Galpin, C. A. Ahern, B. Roux & F. Bezanilla. Intermediate state trapping of a voltage sensor, *Journal of General Physiology* **140**, 635-652 (2012).
20. O. S. Smart, J. G. Neduvelil, X. Wang, B. A. Wallace & M. S. P. Sansomt. HOLE: A program for the analysis of the pore dimensions of ion channel structural models. (1996).
21. J. J. Lacroix & F. Bezanilla. Control of a final gating charge transition by a hydrophobic residue in the S2 segment of a K+ channel voltage sensor, **108** (2011).
22. J. J. Lacroix, F. V. Campos, L. Frezza & F. Bezanilla. Molecular bases for the asynchronous activation of sodium and potassium channels required for nerve impulse generation, *Neuron* **79**, 651-657 (2013).
23. W. Treptow, Y. Liu, C. A. Z. Bassetto, B. I. Pinto, J. A. Alves Nunes, R. M. Uriarte, C. J. Chipot, F. Bezanilla & B. Roux. Isoleucine gate blocks K+ conduction in C-type inactivation, *eLife* **13** (2024).
24. C. J. Peters, D. Fedida & E. A. Accili. Allosteric coupling of the inner activation gate to the outer pore of a potassium channel, *Scientific Reports* **3** (2013).
25. Q. Li, S. Wanderling, M. Paduch, D. Medovoy, A. Singharoy, R. McGreevy, C. A. Villalba-Galea, R. E. Hulse, B. Roux, K. Schulten, A. Kossiakoff & E. Perozo. Structural mechanism of voltage-dependent gating in an isolated voltage-sensing domain, *Nat Struct Mol Biol* **21**, 244-252 (2014).
26. K. McCormack, M. A. Tanouye, L. E. Iverson, J.-W. Lin, M. Ramaswami, T. McCormack, J. T. Campanelli, M. K. Mathew & B. Rudy. A role for hydrophobic residues in the voltage-dependent gating of Shaker K+ channels. 2931-2935 (1991).
27. K. McCormack, L. Lin & F. J. Sigworth. Substitution of a hydrophobic residue alters the conformational stability of Shaker K+ channels during gating and assembly, *Biophys J* **65**, 1740-1748 (1993).
28. N. E. Schoppa, K. McCormack, M. A. Tanouye & F. J. Sigworth. The size of gating charge in wild-type and mutant Shaker potassium channels, *Science* **255**, 1712-1715 (1992).
29. E. Perozo, R. Mackinnon, F. Bezanilla, E. Stefanis & J. Stein. Gating Currents from a Nonconducting Mutant Reveal Open-Closed Conformations in Shake; K+ Channels. 353-358 (1993).
30. E. Perozo, L. Santacruz-Toloza, E. Stefani, F. Bezanilla & D. M. Papazian. S4 mutations alter gating currents of Shaker K channels, *Biophysical Journal* **66**, 345-354 (1994).
31. T. Hoshi, W. N. Zagotta & R. W. Aldrich. Shaker potassium channel gating. I: Transitions near the open state, *The Journal of general physiology* **103**, 249-278 (1994).
32. W. N. Zagotta, T. Hoshi, J. Dittman & R. W. Aldrich. Shaker potassium channel gating. II: Transitions in the activation pathway, *The Journal of general physiology* **103**, 279-319 (1994).
33. W. N. Zagotta, T. Hoshi & R. W. Aldrich. Shaker Potassium Channel Gating Evaluation of Kinetic Models for Activation III. (1994).
34. W. Wang & B. A. Malcolm. Two-stage PCR protocol allowing introduction of multiple mutations, deletions and insertions using QuikChange(TM) Site-Directed Mutagenesis, *BioTechniques* **26**, 680-682 (1999).
35. T. Hoshi, W. N. Zagotta & R. W. A. Howard. Two Types of Inactivation in Shaker K+ Channels: Effects of Alterations in the Carboxy-Terminal Region. 547-556 (1991).

36. A. Punjani, J. L. Rubinstein, D. J. Fleet & M. A. Brubaker. CryoSPARC: Algorithms for rapid unsupervised cryo-EM structure determination, *Nature Methods* **14**, 290-296 (2017).
37. A. Punjani, H. Zhang & D. J. Fleet. Non-uniform refinement: adaptive regularization improves single-particle cryo-EM reconstruction, *Nature Methods* **17**, 1214-1221 (2020).
38. P. Emsley, B. Lohkamp, W. G. Scott & K. Cowtan. Features and development of Coot, *Acta Crystallographica Section D: Biological Crystallography* **66**, 486-501 (2010).
39. T. I. Croll. ISOLDE: A physically realistic environment for model building into low-resolution electron-density maps, *Acta Crystallographica Section D: Structural Biology* **74**, 519-530 (2018).
40. T. D. Goddard, C. C. Huang, E. C. Meng, E. F. Pettersen, G. S. Couch, J. H. Morris & T. E. Ferrin. UCSF ChimeraX: Meeting modern challenges in visualization and analysis, *Protein Science* **27**, 14-25 (2018).
41. E. F. Pettersen, T. D. Goddard, C. C. Huang, E. C. Meng, G. S. Couch, T. I. Croll, J. H. Morris & T. E. Ferrin. UCSF ChimeraX: Structure visualization for researchers, educators, and developers, *Protein Science* **30**, 70-82 (2021).
42. P. V. Afonine, B. K. Poon, R. J. Read, O. V. Sobolev, T. C. Terwilliger, A. Urzhumtsev & P. D. Adams. Real-space refinement in PHENIX for cryo-EM and crystallography, *Acta Crystallographica Section D: Structural Biology* **74**, 531-544 (2018).
43. S. Enrico & B. Francisco. Cut-Open Oocyte Voltage-Clamp Technique, *METHODS IN ENZYMOLOGY* **293** (1998).
44. J. Jumper, R. Evans, A. Pritzel, T. Green, M. Figurnov, O. Ronneberger, K. Tunyasuvunakool, R. Bates, A. Žídek, A. Potapenko, A. Bridgland, C. Meyer, S. A. A. Kohl, A. J. Ballard, A. Cowie, B. Romera-Paredes, S. Nikolov, R. Jain, J. Adler, T. Back, S. Petersen, D. Reiman, E. Clancy, M. Zielinski, M. Steinegger, M. Pacholska, T. Berghammer, S. Bodenstein, D. Silver, O. Vinyals, A. W. Senior, K. Kavukcuoglu, P. Kohli & D. Hassabis. Highly accurate protein structure prediction with AlphaFold, *Nature* **596**, 583-589 (2021).
45. R. Evans, M. O'Neill, A. Pritzel, N. Antropova, A. Senior, T. Green, A. Žídek, R. Bates, S. Blackwell, J. Yim, O. Ronneberger, S. Bodenstein, M. Zielinski, A. Bridgland, A. Potapenko, A. Cowie, K. Tunyasuvunakool, R. Jain, E. Clancy, P. Kohli, J. Jumper & D. Hassabis. (2021).
46. M. Mirdita, K. Schütze, Y. Moriwaki, L. Heo, S. Ovchinnikov & M. Steinegger. ColabFold: making protein folding accessible to all, *Nature Methods* **19**, 679-682 (2022).
47. S. O & et al. (Github repository, 2025).
48. H. K. Wayment-Steele, A. Ojoawo, R. Otten, J. M. Apitz, W. Pitsawong, M. Hömberger, S. Ovchinnikov, L. Colwell & D. Kern. Predicting multiple conformations via sequence clustering and AlphaFold2, *Nature* **625**, 832-839 (2024).
49. P. Eastman, R. Galvelis, R. P. Peláez, C. R. A. Abreu, S. E. Farr, E. Gallicchio, A. Gorenko, M. M. Henry, F. Hu, J. Huang, A. Krämer, J. Michel, J. A. Mitchell, V. S. Pande, J. P. Rodrigues, J. Rodriguez-Guerra, A. C. Simmonett, S. Singh, J. Swails, P. Turner, Y. Wang, I. Zhang, J. D. Chodera, G. De Fabritiis & T. E. Markland. OpenMM 8: Molecular Dynamics Simulation with Machine Learning Potentials, *Journal of Physical Chemistry B* **128**, 109-116 (2024).
50. B. R. Brooks, C. L. Brooks, A. D. Mackerell, L. Nilsson, R. J. Petrella, B. Roux, Y. Won, G. Archontis, C. Bartels, S. Boresch, A. Caflisch, L. Caves, Q. Cui, A. R. Dinner, M. Feig, S. Fischer, J. Gao, M. Hodoscek, W. Im, K. Kuczera, T. Lazaridis, J. Ma, V. Ovchinnikov, E. Paci, R. W. Pastor, C. B. Post, J. Z. Pu, M. Schaefer, B. Tidor, R. M. Venable, H. L. Woodcock, X. Wu, W. Yang, D. M. York & M. Karplus. CHARMM: The biomolecular simulation program, *Journal of Computational Chemistry* **30**, 1545-1614 (2009).
51. J. Huang, S. Rauscher, G. Nawrocki, T. Ran, M. Feig, B. L. De Groot, H. Grubmüller & A. D. MacKerell. CHARMM36m: An improved force field for folded and intrinsically disordered proteins, *Nature Methods* **14**, 71-73 (2016).
52. R. B. Best, X. Zhu, J. Shim, P. E. M. Lopes, J. Mittal, M. Feig & A. D. MacKerell. Optimization of the additive CHARMM all-atom protein force field targeting improved sampling of the backbone φ, ψ and side-chain χ1 and χ2 Dihedral Angles, *Journal of Chemical Theory and Computation* **8**, 3257-3273 (2012).
53. A. D. MacKerell, M. Feig & C. L. Brooks. Improved Treatment of the Protein Backbone in Empirical Force Fields, *Journal of the American Chemical Society* **126**, 698-699 (2004).
54. A. D. MacKerell Jr, D. Bashford, M. Bellott, R. L. Dunbrack Jr, J. D. Evanseck, M. J. Field, S. Fischer, J. Gao, H. Guo & S. Ha. All-atom empirical potential for molecular modeling and dynamics studies of proteins, *The journal of physical chemistry B* **102**, 3586-3616 (1998).

55. J. B. Klauda, R. M. Venable, J. A. Freites, J. W. O'Connor, D. J. Tobias, C. Mondragon-Ramirez, I. Vorobyov, A. D. MacKerell & R. W. Pastor. Update of the CHARMM All-Atom Additive Force Field for Lipids: Validation on Six Lipid Types, *Journal of Physical Chemistry B* **114**, 7830-7843 (2010).
56. D. Beglov & B. Roux. Finite representation of an infinite bulk system: Solvent boundary potential for computer simulations, *The Journal of Chemical Physics* **100**, 9050-9063 (1994).
57. W. L. Jorgensen, J. Chandrasekhar, J. D. Madura, R. W. Impey & M. L. Klein. Comparison of simple potential functions for simulating liquid water, *The Journal of Chemical Physics* **79**, 926-935 (1983).
58. S. Jo, T. Kim, V. G. Iyer & W. Im. CHARMM-GUI: A web-based graphical user interface for CHARMM, *Journal of Computational Chemistry* **29**, 1859-1865 (2008).
59. E. L. Wu, X. Cheng, S. Jo, H. Rui, K. C. Song, E. M. Dávila-Contreras, Y. Qi, J. Lee, V. Monje-Galvan, R. M. Venable, J. B. Klauda & W. Im. in *Journal of Computational Chemistry* Vol. 35 1997-2004 (John Wiley and Sons Inc., 2014).
60. S. Jo, T. Kim & W. Im. Automated builder and database of protein/membrane complexes for molecular dynamics simulations, *PLoS ONE* **2** (2007).
61. S. Jo, J. B. Lim, J. B. Klauda & W. Im. CHARMM-GUI membrane builder for mixed bilayers and its application to yeast membranes, *Biophysical Journal* **97**, 50-58 (2009).
62. S. Bernèche & B. Roux. Energetics of ion conduction through the K+ channel, *Nature* **414**, 73-77 (2001).
63. W. Humphrey, A. Dalke & K. Schulten. VMD: Visual molecular dynamics, *Journal of Molecular Graphics* **14**, 33-38 (1996).
64. B. Roux. The membrane potential and its representation by a constant electric field in computer simulations, *Biophysical Journal* **95**, 4205-4216 (2008).
65. F. Khalili-Araghi, V. Jogini, V. Yarov-Yarovoy, E. Tajkhorshid, B. Roux & K. Schulten. Calculation of the gating charge for the Kv1.2 voltage-activated potassium channel, *Biophysical Journal* **98**, 2189-2198 (2010).